

# PCCP

Accepted Manuscript



This is an *Accepted Manuscript*, which has been through the Royal Society of Chemistry peer review process and has been accepted for publication.

*Accepted Manuscripts* are published online shortly after acceptance, before technical editing, formatting and proof reading. Using this free service, authors can make their results available to the community, in citable form, before we publish the edited article. We will replace this *Accepted Manuscript* with the edited and formatted *Advance Article* as soon as it is available.

You can find more information about *Accepted Manuscripts* in the [Information for Authors](#).

Please note that technical editing may introduce minor changes to the text and/or graphics, which may alter content. The journal's standard [Terms & Conditions](#) and the [Ethical guidelines](#) still apply. In no event shall the Royal Society of Chemistry be held responsible for any errors or omissions in this *Accepted Manuscript* or any consequences arising from the use of any information it contains.

**Influence of Gas Packing and Orientation on FTIR activity for CO  
chemisorption to the Cu Paddlewheel**

**Cheng-Yu Wang<sup>a</sup>, Paramita Ray<sup>b</sup>, Qihan Gong<sup>c</sup>, Yonggang Zhao<sup>c</sup>, Jing Li<sup>c</sup>,  
Angela D. Lueking<sup>a,\*</sup>**

<sup>a</sup>Departments of Energy and Mineral Engineering & Chemical Engineering; EMS Energy Institute,

<sup>b</sup>Department of Chemistry, Pennsylvania State University, University Park, PA 16802, USA

<sup>c</sup>Department of Chemistry & Chemical Biology, Rutgers University, Piscataway, NJ 08854, USA

\* Corresponding author. Email: [adl11@psu.edu](mailto:adl11@psu.edu)  
Telephone: (814) 863-6256; Fax: (814) 865-7846

**Abstract**

*In situ* Fourier-transform infrared (FTIR) spectroscopy is able to probe structural defects via site-specific adsorption of CO to the Cu-BTC (BTC = 1,3,5-benzenetricarboxylate) metal-organic framework (MOF). The temperature-programmed desorption (TPD) of CO chemisorbed to Cu-TDPAT (TDPAT = 2,4,6-tris(3,5-dicarboxylphenylamino)-1,3,5-triazine) is virtually identical to Cu-BTC, suggesting CO chemisorbs to the open metal site at the axial position of the copper paddlewheel that is the building unit of both MOFs. Yet, despite an increased gravimetric CO:Cu ratio, CO chemisorbed to Cu-TDPAT is FTIR inactive. We rule out the presence of residual solvent, thermal degradation, adsorption temperature, and ligand-induced electronic effects at the adsorption site. TPD at increased pressure suggests the multiple CO per Cu site rearrange in Cu-TDPAT as a dynamic function of temperature and pressure. Thus, the FTIR inactivity of CO chemisorbed to CuTDPAT is attributed to orientation and/or packing of the CO relative to the Cu binding site. The results suggest dynamic chemisorption complicate extension of a site-specific *in situ* FTIR probe of gas adsorption. For both Cu-BTC and Cu-TDPAT, the *in situ* FTIR probe is a less sensitive probe of defects than X-ray photoelectron spectroscopy and nitrogen adsorption.

Keywords: Metal-organic frameworks, adsorption, chemisorption, Fourier-transform infrared spectroscopy, defects

## 1. Introduction

Metal-organic frameworks (MOFs) are comprised of metal clusters linked by organic ligands that lead to crystalline structures with long range order. Different combinations of metal clusters and ligand lead to almost an unlimited variation in the accessible free space, surface area, pore dimension, and chemical topology.<sup>1</sup> High porosity, large surface area, and tunable porosity make MOFs ideally suited for gas separation and storage,<sup>1-4</sup> drug delivery,<sup>5</sup> chemical sensing,<sup>6,7</sup> and catalysis.<sup>8,9</sup> Performance of MOFs in these applications is determined by the affinity between the MOF “host” and the guest species, which can be further tuned by pre- or post-synthesis modification strategies, from varying the organic ligand,<sup>10,11</sup> to catenation,<sup>12</sup> functionalization,<sup>13-15</sup> and addition of alkali sites.<sup>16</sup> Defects may also be unintentionally generated by missing ligands in the framework,<sup>17-19</sup> or intentionally generated by altering the nature of the carboxylate - metal bond,<sup>20</sup> thermal annealing,<sup>21,22</sup> or using mixed ligands to build the framework.<sup>23,24</sup> There is an increasing realization that defects in MOFs may play a critical role in the affinity of the MOF host to accommodate a guest, as well as material stability. Thus, understanding the effect of defects is very important in developing high performance MOFs for the applications outlined above. *In situ* spectroscopy, in particular, has the potential to provide site-specific information of defects at the condition of measurement. Interestingly, our results reported here suggest spectroscopic measurements are not easily extrapolated from one MOF to another, even when the binding sites are quite similar. The somewhat surprising finding suggests a dynamic gas-surface interaction, even when the gas is chemisorbed.

The structural quality of MOFs is most often characterized by powder X-ray diffraction (PXRD). Hafizovic et al. found defects from interpenetration or partial

disconnection of the linkage between the metal cluster and organic ligand led to peak splitting and change in the ratio of intensity of the various diffraction peaks.<sup>25</sup>

However, it is often quite difficult to assess the extent of defects and MOF structural quality by PXRD alone. In a previous study,<sup>26</sup> we embedded a catalyst (platinum on activated carbon) into three MOFs by introducing the catalyst into a solution of the MOF precursors prior to crystallization. After embedding a secondary particle within the crystal structure, the only evidence in PXRD for this significant heterogeneity was a very slight shift in the diffraction peaks relative to the unmodified crystal, with no evidence for peak splitting or noticeable changes in intensity. Catalyst insertion was also undetectable via nitrogen adsorption isotherms, Fourier Transform infrared spectroscopy (FTIR), or X-ray photoelectron spectroscopy (XPS). Although we noted some loss of surface area after rapid pressurization in helium or hydrogen (from 0 to 80 bar), the PXRD pattern remained unchanged even with the surface area loss. The loss of surface area was observed for MOFs with inserted catalyst, as well as seemingly perfect unaltered structures. We suspect these innate defects correlated to increased hydrogen chemisorption, perhaps facilitating nucleation of hydrogenation of the ligand. Similarly, Tsao et al. found creation of a fractal porous network, perhaps stimulated by physical grinding, facilitated catalysis and hydrogenation of the framework.<sup>27</sup> Variation of the local metal coordination in different batches of Cu-BTC (copper 1,3,5-benzenetricarboxylate, a.k.a.  $\text{Cu}_3(\text{BTC})_2$  or HKUST), despite identical PXRD patterns, gave rise to increased catalytic activity in the conversion of  $\alpha$ -pinene oxide.<sup>28</sup>

*In situ* FTIR spectroscopy is emerging to probe structural defects in gas (e.g. CO) adsorbed MOFs, particularly those that contain open-metal sites such as Cu-BTC.<sup>22,29,30</sup> The Cu paddlewheel (PDW) in Cu-BTC consists of a  $\text{Cu}^{2+}$  dimer

covalently bound to four carboxylate groups that terminate the benzene tricarboxylate ligand; repetition of this bonding arrangement gives rise to a porous framework with square pores that are approximately 9 Å by 9 Å<sup>31,32</sup> (Figure 1). Removal of water molecules coordinated to the axial position via a mild thermal evacuation gives rise to open metal sites that adsorb small molecules with a fairly strong binding energy, i.e. the CO binding energy to the Cu-axial position was calculated to be 0.290 eV by density functional theory (DFT) using a truncated Cu<sub>2</sub>(BTC)<sub>4</sub> analog structure.<sup>22</sup>

Free gas-phase CO has 2 peaks at ~2120 and ~2170 cm<sup>-1</sup>, corresponding to the R branch vibrational transition and P branch rotational transition, with a cleft at 2143 cm<sup>-1</sup>, a transition that is forbidden for diatomic molecules under infrared selection rules.<sup>33</sup> When associated with a surface, the vibrational modes of CO become perturbed, as a Cu-CO type ionic carbonyl is formed, which is sensitive to the Cu oxidation state and the presence of nearby CO species. This technique was used to characterize Cu-containing surfaces well before the development of MOFs. For example, adsorption of CO to 1 wt% CuO/SiO<sub>2</sub> gave rise to a perturbation of the CO IR spectra: peaks at 2216, 2199, and 2180 cm<sup>-1</sup> were attributed to CO adsorption to Cu<sup>2+</sup>, whereas a feature at 2126.5 cm<sup>-1</sup> was attributed to CO adsorption to Cu<sup>+</sup>.<sup>34</sup> Adsorption of CO to the Cu<sup>+</sup> species in copper zeolite (Cu-ZSM-5) gave rise to a mode at 2137 cm<sup>-1</sup>, which was augmented with additional modes at 2177.5 and 2151 cm<sup>-1</sup> with increased CO surface coverage that were assigned to dicarbonyl Cu<sup>+</sup>(CO)<sub>2</sub> species.<sup>34</sup>

Adsorption of CO to the Cu<sup>2+</sup> axial position of Cu-BTC gives rise to a perturbation in the CO spectra at ~2170 cm<sup>-1</sup>.<sup>21,22,28,35</sup> An additional feature, typically at ~2120 cm<sup>-1</sup> is an indication of CO interacting with Cu<sup>+</sup>, and the origin of this Cu<sup>+</sup> site is more controversial. Both Alaerts et al.<sup>28</sup> and Szanyi et al.<sup>30</sup> claimed CO

adsorption led to reduction of Cu (from  $\text{Cu}^{2+}$  to  $\text{Cu}^+$ ), particularly as the intensity of this mode increased with time at moderate temperatures but not at low temperatures ( $<150$  K).<sup>30</sup> Bordiga et al. attributed this to trace amounts of  $\text{Cu}_2\text{O}$  impurities.<sup>35</sup> Using DFT, StPetkov et al. demonstrated the  $\text{Cu}^+$  mode was consistent with a defect formed by the removal of a ligand.<sup>22</sup>

The original intent of this work was to extend the FTIR CO adsorption technique from Cu-BTC to Cu-TDPAT (TDPAT = 2,4,6-tris(3,5-dicarboxylphenylamino)-1,3,5-triazine or  $\text{Cu}_3(\text{TDPAT})$ ). Like Cu-BTC, Cu-TDPAT is built from the Cu PDW structure. Substitution of the BTC ligand for TDPAT leads to three cages with diameters estimated to be 9.1, 12, and 17.2 Å.<sup>36</sup> Although the pore structure of Cu-TDPAT is a bit more complex (see Figure 1), we anticipated chemisorption of CO to the axial Cu binding positions of the Cu PDW within the framework would be similar. Although we found evidence for increased CO adsorption in Cu-TDPAT via gravimetric techniques, we found no corresponding evidence for perturbation of the CO spectra in FTIR. To explain this apparent anomaly, we explore the effect of both introduced and inherent defects on the *in situ* CO FTIR probe, and compare this probe to more traditional characterization methods of gas adsorption, XRD, XPS, and temperature-programmed desorption. Our results suggest dynamic realignment of the adsorbed layer and a high sensitivity to the orientation of the adsorbed layer.

## 2. Experimental

### 2.1 Sample Preparation

Basolite C300, a.k.a. Cu-BTC, obtained from Sigma-Aldrich (SA) is abbreviated as **B(SA)**, and Cu-BTC obtained from Rutgers University is abbreviated **B(RU)**. **B(RU)** was prepared in a microwave reaction<sup>37</sup> of 0.81 mmol copper nitrate precursor and 0.6 mmol 1,3,5-benzene tricarboxylic acid in 6 ml DMF (Dimethylformamide) at 413 K for 1 hr. The crystals were collected and washed with DMF, and further exchanged with ethanol every 1 hr for one week. FTIR of **B(RU)** was collected after storage in an inert (Ar) environment for over one year prior (abbreviated **B(RU)**-1) the experiments herein, and over time, the color changed from a deep blue to a more vibrant blue (See Figure S10, Supporting Information). The remaining characterization data was collected for both **B(RU)** and **B(RU)**-1.

Cu-TDPAT (**T**) was prepared following previously reported procedures.<sup>36</sup> In brief, solvothermal procedures used 0.68 mmol copper nitrate precursor, 0.05 mmol H<sub>6</sub>TDPAT in 2 ml DMA (Dimethylacetamide), 2 ml DMSO (Dimethyl sulfoxide), 0.2 ml H<sub>2</sub>O, and 0.9 ml HBF<sub>4</sub> at 358 K for three days. The blue polyhedron crystals were washed with DMA and exchanged with methanol every 1 hr during daytime for one week.

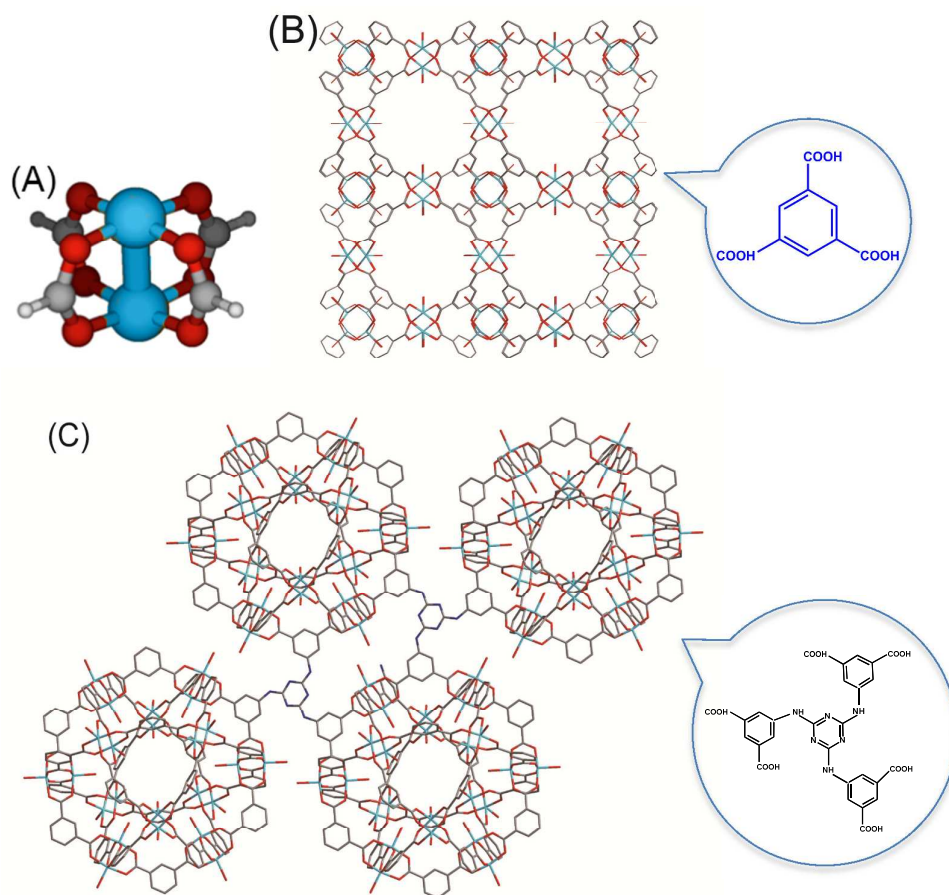


Figure 1. Diagram of copper paddlewheel (Cu PDW) (A), Cu-BTC (B), and Cu-TDPAT (C), in which Cu PDW is a metal cluster, while TDPAT and BTC serve as the organic linkers to connect with metal cluster and form the long-range order MOF structure. (Gray: C, Red: O, Cyan: Cu, Blue: N)

## 2.2 Characterization

The powder X-ray diffraction (PXRD) patterns were collected from PANalytical XPert Pro MPD multipurpose powder diffractometer with a Cu K $\alpha$  ( $\lambda = 1.543 \text{ \AA}$ ) X-ray source, using  $2\theta$  from  $5^\circ$  to  $70^\circ$  at 45 kV, 40 mA, step size  $0.026^\circ$ , and scan speed  $0.067^\circ/\text{sec}$ , with MOF powders on a silica disk. The textural properties of

MOFs were determined by nitrogen physisorption isotherms at 77 K up to 1 bar, obtained on a Micromeritics ASAP 2020 unit. The gas adsorption measurements were preceded by pretreatment at high vacuum ( $<10 \mu\text{mHg} = 10^{-2} \text{ mbar}$ ) at elevated temperature (Cu-BTC: 423 K for 10 hr, and Cu-TDPAT: 393 K for 10 hr, based on TGA data<sup>38</sup>). BET surface area<sup>39</sup> was determined with the relative pressure range ( $P/P_0$ ) from 0 to 0.04, with zeolite- $\text{N}_2$  surface interaction parameters.<sup>2</sup> Total pore volume was calculated by single point adsorption at  $P/P_0 = 0.99$ . Micropore volume was estimated from H-K model (Horváth-Kawazoe equations) with carbon cylindrical pore parameters.<sup>2</sup> Pore size exceeding 20 Å was estimated from BJH model ( $P/P_0$  ranging from 0.001-0.99).<sup>40</sup>

X-ray photoelectron spectroscopy (XPS) used a Kratos Axis Ultra with a monochromatic Al  $K\alpha$  X-ray source operated at 14 kV and 20 mA in hybrid slot mode. The samples were placed on carbon tape to fixate the material to either copper or silicon wafers. In the high-resolution scan we used a pass energy of 20 eV and a step size of 0.1 eV. Surface residual charges in high-resolution spectra were corrected based on C 1s assigned to 284.5 eV. The peak assignment were based on the Handbook of X-Ray Photoelectron Spectroscopy.<sup>41</sup>

The room temperature FTIR spectra were measured in a Bruker IFS 66/S Spectrometer in transmittance mode to confirm 2000 to 2300  $\text{cm}^{-1}$  window in MOFs for further CO spectra. The MOF samples were pressed with KBr to form pellets with a quick press handle and a die set. The low temperature (100 and 150 K) *in situ* FTIR spectra in CO (and Ar) were obtained on a Bruker Hyperion 3000 Microscope using a Linkam stage (THMS600PS Pressure System). The aperture has the diameter 1.3 mm, and the stage has top and bottom IR permeable ZnSe window adaption. MOF powders were pressed on to a 400-mesh TEM grid with a quick press handle and a die

set, and then placed on the Linkam stage aperture. After an Ar purge to remove air, the MOF samples were pretreated *in situ* at high temperature in ~0.34 bar Ar gas flow. The pretreatment temperature was varied (from 373 K to 633 K; see Table S1, Supporting Information) to retain coordinated water molecules or introduce thermal degradation, as discussed below. In all cases, the samples were then cooled to either 100 K or 150 K, temperatures that were previously found to minimize Cu reduction.<sup>30</sup> The following spectra were collected in sequence at constant temperature, with the numbers referring to labels in the figures below: (0) an initial baseline spectrum in Ar, (1) introduction of 0.34 bar CO (labeled as “excess CO”), (2-3) stabilization of the spectra in 0.34 CO to ensure steady state, (4-further spectra) subsequent Ar purging, anticipated to remove gaseous and physisorbed CO, while chemisorbed CO was retained (labeled “CO chemisorption”), and in select cases, the temperature was subsequently raised (in flowing Ar) to probe the desorption temperature of strongly bound CO. This last step is referred to as temperature-desorption FTIR (TD-FTIR) below. Multiple FTIR spectra were collected to ensure there were no changes in the spectra with time, and the labels below refer to sequential measurements with time, (separated by ~10 minutes, see also Supporting Information, Figure S2). The pressure of 0.34 bar was chosen as it corresponds to the  $10^{-5}$  molar dosing used by Szanyi et al.<sup>30</sup> for our system volume. Peak positions discussed below were determined via fitting with a Gaussian-Lorentzian mixed function (fitting parameters: position, intensity, FWHM, and Gaussian-Lorentzian ratio) with Shirley background fitting.

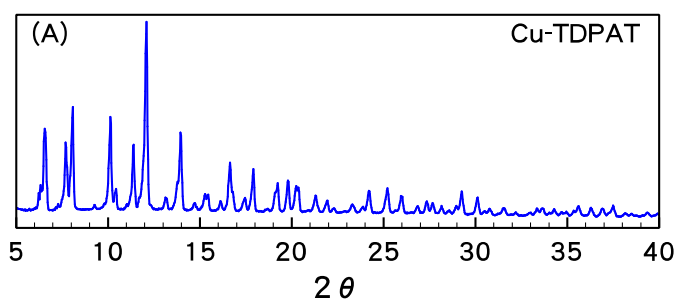
CO adsorption isotherms and temperature-programmed desorption (TPD) spectra were collected at comparable conditions using a Hiden thermogravimetric analyzer IGA-001. After pretreatment (Cu-BTC: 423 K for 10 hr, and Cu-TDPAT: 393 K for 10 hr), the temperature was cooled to 300 K under high vacuum ( $10^{-5}$  torr),

and then immersed in liquid nitrogen to bring the system temperature to 77 K. An adsorption isotherm up to 0.34 bar CO at 77 K ( $P/P_0 = 0.59$ ) was performed to match the conditions of the FTIR experiments. After CO adsorption, the temperature was raised from 77 K to 300 K (at approximately 2 K/min), by manually lowering the liquid nitrogen bath. This TPD experiment was performed in both high vacuum ( $10^{-5}$  torr) and in a closed system of 0.34 bar CO. Unlike the FTIR measurements, CO was used instead of Ar as our IGA system is not currently set-up for immediate gas switching. Sample weights were corrected for buoyancy effects based on density measurements from helium isotherms at 300 K to 20 bar. The molar ratio of CO adsorbed/desorbed was normalized to both total pore volume, and to the amount of Cu present in each MOF based on the theoretical formula unit (3 Cu atoms in 1 MOF unit cell). In TPD, the normalized weight derivative was calculated with effective interval 20 points span ( $\sim 1$  K in x-axis). TPD data was normalized to the weight prior to introduction of CO. The sample weight was converted to the amount of Cu using the ideal stoichiometric formula to reflect the adsorption at the axial positions of interest. For estimation of activation energy from the TPD profile with a Redhead analysis (see Supporting Information), the temperature at which desorption was a maximum was determined via curve fitting of the derivative of the TPD derivative profile.

### 3. Results and Discussion

#### 3.1 Structural Characterization

PXRD analysis and N<sub>2</sub> adsorption isotherms indicate the samples are robust, with high crystallinity and surface area. The experimental PXRD patterns of Cu-TDPAT (**T**) and both sources of Cu-BTC, i.e. **B**(RU) and **B**(SA) (Figure 2), match the expected patterns (**T**<sup>36</sup> and **B**<sup>18,38,42</sup>), with no signs of peak splitting and/or variation in the relative peak intensities that would be indicative of structural degradation.<sup>25</sup> As reported elsewhere, neither Cu-TDPAT<sup>36</sup> or Cu-BTC<sup>37</sup> have appreciable changes in their PXRD patterns when coordinated water molecules are removed. As only minor variations in relative intensities are observed between **B**(RU) and **B**(SA), PXRD is fairly insensitive to the different synthesis procedures. A subtle difference was noted in the relative peak intensity ratios of **B**(RU) relative to of aged **B**(RU)-1, with the relative intensity of the first peak increased by 50% (Figure 2B), but no peak splitting was observed.



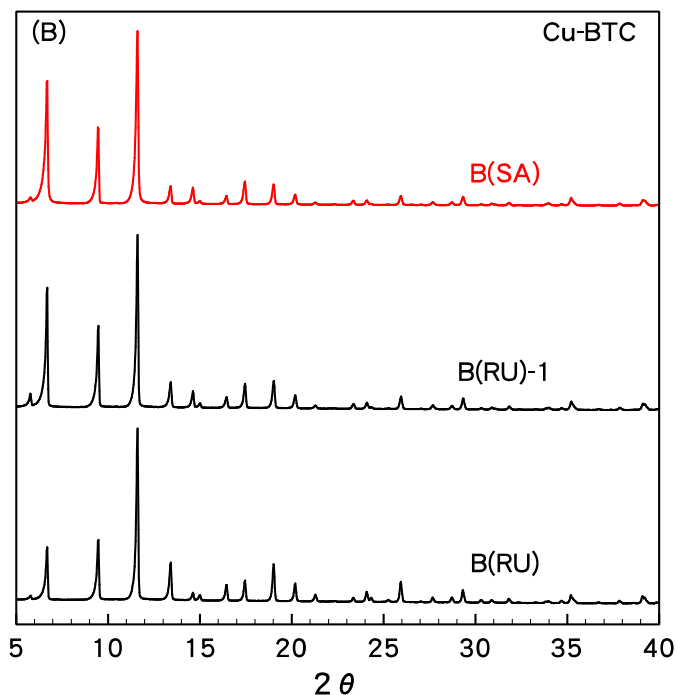


Figure 2. The PXRD of Cu-TDPAT (A) and Cu-BTC (B) series. The diffraction peak positions agree with the literature.<sup>18,36,38</sup> Note that the relative intensity of the first peak of **B(RU)-1** ( $2\theta = 6.7^\circ$ ) is increased by 50% relative to **B(RU)**.

The reversible 77 K nitrogen isotherms of **B** (Figure 3) are typical of a microporous samples. Three distinct steps in the type-VI isotherm<sup>40</sup> are indicative of filling of three adsorption sites with distinct binding energies. The steps cannot be attributed to differences in pore size, as the crystal structure of **B** has uniform, semi-spherical pores along all dimensions (Figure 1). No significant differences are found in the N<sub>2</sub> isotherms of **B(RU)** and **B(SA)**, despite different sources for these materials and the scale of synthesis used. Differences in the corresponding BET surface areas are 1770 m<sup>2</sup>/g and 1760 m<sup>2</sup>/g for **B(RU)** and **B(SA)**, respectively, well within the error of the measurement. The increased surface area relative to previous reports (i.e.

1.2~1.5-fold of those reported previously<sup>37,42</sup>) reflects the sensitivity of the BET analysis to the selected pressure range. The BET surface area of the aged **B**(RU)-1 was 1600 m<sup>2</sup>/g, reduced by 10% relative to the **B**(RU) precursor; with a similar reduction in total pore volume (Table 1). The pore-size distribution (PSD) of all **B** samples estimated via the Horvath-Kawazoe (H-K) method suggests the pores of **B** are <12 Å and 14 – 17 Å (Figure S8, Supporting Information).

The N<sub>2</sub> isotherm of **T** lacks the distinct steps in the N<sub>2</sub> adsorption isotherm. The calculated BET surface area of **T** is 1640 m<sup>2</sup>/g (Table 1), ~85% of a previously reported value.<sup>36</sup> It is notable that the **T** isotherm lacks distinct steps, despite a crystalline structure with two distinct pores sizes (Figure 1). The calculated H-K PSD of **T** is quite broad, with pore sizes ranging from 10 – 20 Å (Figure S8).

XPS spectra of **B**(SA) consisted of a major (88%) Cu<sup>2+</sup> peak at 934.5 eV, and a small (12%) reduced Cu<sup>+</sup>/Cu<sup>0</sup> peak at 932.4 eV (Figure 4). The spectra of **B**(RU) was very similar with a Cu<sup>2+</sup>:Cu<sup>+</sup>/Cu<sup>0</sup> of 89:11, within the error of measurement. With aging, the fraction of Cu<sup>+</sup>/Cu<sup>0</sup> in the sample increased by 6%, with a Cu<sup>2+</sup>:Cu<sup>+</sup>/Cu<sup>0</sup> of 83:17 for **B**(RU)-1. In the absence of any reduced Cu phase in PXRD (Figure 3), the Cu<sup>+</sup>/Cu<sup>0</sup> peak has been associated with structural defects. The O 1s spectra are included in the Supporting Information (Figure S9), and it reflects the oxidation trends for the Cu spectra. Discussion of the differences between **B**(SA) and **B**(RU) is left for section 3.2.3.

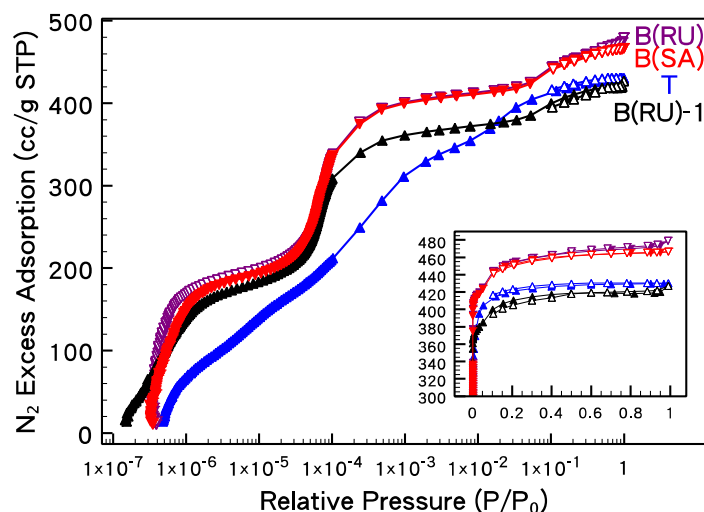


Figure 3. Nitrogen 77 K, 1 bar isotherms of Cu-TDPAT (**T** in blue) and Cu-BTC (**B(SA)** in red, **B(RU)** in purple, and **B(RU)-1** in black).

Table 1. Textural properties of Cu-TDPAT (**T**) and Cu-BTC (**B(SA)**, as-received **B(RU)**, and aged **B(RU)**).

Samples	SA <sub>BET</sub> (m <sup>2</sup> /g)	V <sub>total</sub> (cc/g)	V <sub>micro</sub> (cc/g)	BJH 20Å- 3000Å Ads P/P <sub>0</sub> 0.99 HK cumulated to 20Å (cc/g)	BJH 20Å- 3000Å Des (cc/g)
<b>T</b>	1640	0.67	0.51	0.069	0.039
<b>B(SA)</b>	1760	0.72	0.62	0.061	0.071
<b>B(RU)</b>	1770	0.74	0.62	0.080	0.090
<b>B(RU)-1</b>	1600	0.66	0.56	0.062	0.082

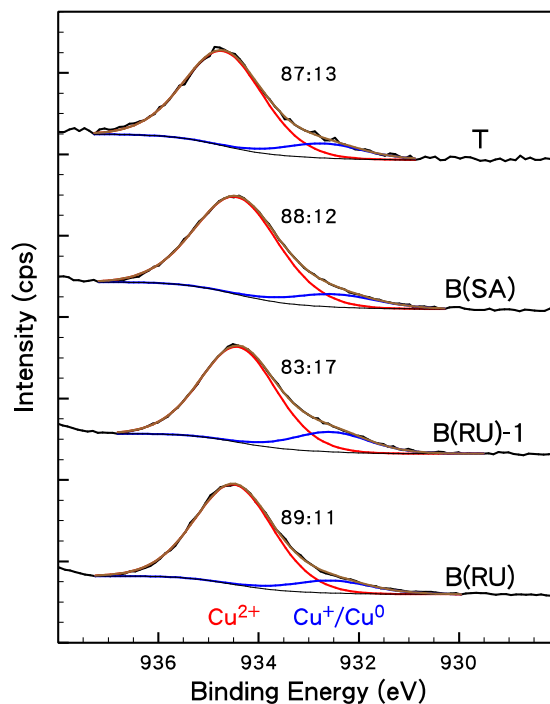


Figure 4. XPS spectra of Cu 2p<sub>3/2</sub> of Cu-BTC **B(RU)**, **B(RU)-1**, **B(SA)**, and Cu-TDPAT (**T**).

### 3.2 In situ CO FTIR measurements of Cu-BTC

#### 3.2.1 CO perturbation by **B(SA)** Cu-BTC

FTIR spectra of **B(SA)** in 0.34 bar CO at 150 K (i.e. spectra (1) to (3), Figure 5A) reproduces previous findings.<sup>21,22,28,35</sup> Specifically, CO perturbations are observed at  $\sim 2120$  and  $\sim 2170$   $\text{cm}^{-1}$ , which are assigned to interactions of CO with  $\text{Cu}^+$  and  $\text{Cu}^{2+}$ , respectively, for reasons discussed previously.<sup>30</sup> In 0.34 bar CO, one would expect the dominant vibrations to be attributed to gas-phase CO, yet there is also a sharp feature in the spectra centered at  $2169$   $\text{cm}^{-1}$  which can be attributed to interaction of CO with **B(SA)**. This feature was not observed in certain defected

samples, discussed subsequently, and demonstrates a portion of the gaseous CO is affected by the electronic environment of the **B(SA)** surface.

As gaseous CO is removed via Ar purging, CO that binds to the surface with an energy greater than the thermal energy is expected to be retained by the surface. Most notably, broad shoulders at 2156 and 2191  $\text{cm}^{-1}$  (see (4), Figure 5A) quickly disappear as excess CO is removed. These shoulders were previously assigned to multiple CO molecules per the  $\text{Cu}^{2+}$  adsorption site,<sup>28,35</sup> but after an isotopic labeling experiment, tentatively reassigned to single CO bound to the organic ligand.<sup>29</sup> After 30 minutes of Ar purging (spectrum (11), Figure 5A), modes at 2172  $\text{cm}^{-1}$  and 2120  $\text{cm}^{-1}$  remain in the spectra (See also peak fitting Figure S3 of the Supporting Information), and are assigned to CO chemisorbed to  $\text{Cu}^{2+}$  and  $\text{Cu}^+$ , respectively, as there is no corresponding gas-phase CO. The red-shift in the CO- $\text{Cu}^+$  mode (from 2123  $\text{cm}^{-1}$  to 2120  $\text{cm}^{-1}$ ) was previously attributed to differences in how CO was interacting with the aromatic ligand.<sup>29</sup> However, we can find no corresponding perturbations in the FTIR spectra of either the organic ligand (Figure S4, Supporting Information) or the Cu-O vibrational modes (Figure S11, Supporting Information) that clarify the role of the ligand. The similarity of the CO TPD profiles of the two materials at 0 bar (discussed below) suggests the CO does not interact strongly with the ligand. The blue-shift in the CO- $\text{Cu}^{2+}$  mode with removal of gaseous CO (from 2169  $\text{cm}^{-1}$  to 2172  $\text{cm}^{-1}$ ) was previously attributed to a decrease in the number of CO interacting with the  $\text{Cu}^{2+}$ ,<sup>29,35</sup> which is consistent with our TPD discussed below that suggest multiple CO per  $\text{Cu}^{2+}$  adsorption site.

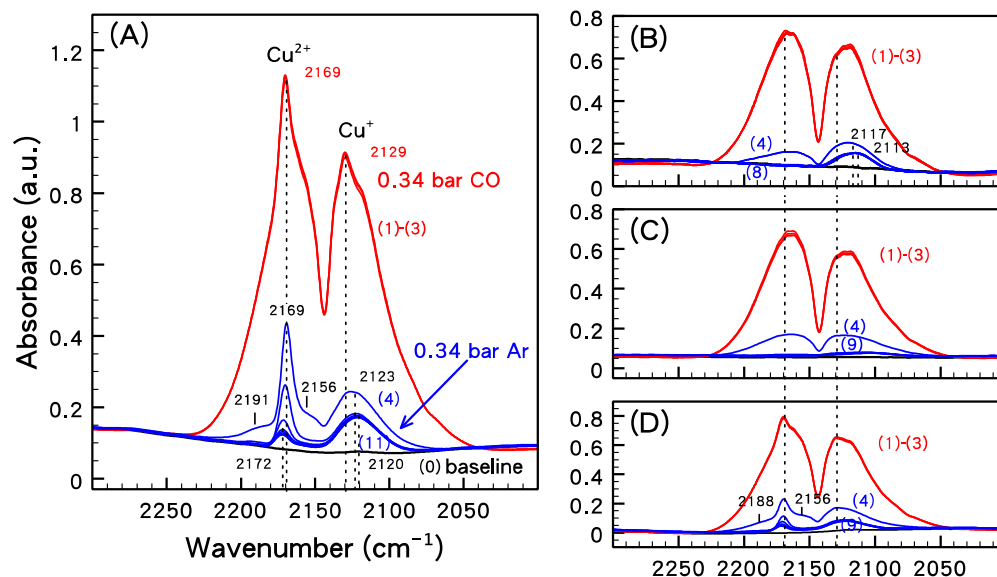


Figure 5. FTIR spectra of (A-C) **B(SA)**, and (D) aged **B(RU)-1** at 150 K in 0.34 bar CO (1-3), and subsequently, in 0.34 bar Ar to retain chemisorbed CO (4-11). The label number represents the sequence of each spectrum, with increasing time. (0) was collected in Ar prior to introduction of CO. **B(SA)** has been subjected to the following variations in pretreatment: (A) 543 K for 1 minute to removed coordinated water; (B) no heating to retain coordinated water; and (C) 633 K for 1 minute to induce thermal degradation. In (D), **B(RU)** was “aged” in an inert atmosphere for one year, and then pretreated at 543 K for 1 minute prior to the FTIR measurement. The dotted lines are meant to guide the eye, and are at positions of 2169 and 2129  $\text{cm}^{-1}$  in both panels.

### 3.2.2 CO perturbation by **B(SA)** Cu-BTC with introduced defects

We next explored how residual water, coordinated to the axial  $\text{Cu}^{2+}$  position, would influence the CO FTIR spectra in the presence of **B(SA)**. This serves as a means to introduce a “defect” (i.e. residual solvent) into the structure, as well as a control experiment for the **T** measurements of the next section. To retain water, the

thermal pretreatment was eliminated, and water retention was confirmed with a strong OH stretch in FTIR (See Supporting Information, Figure S6A). The presence of residual water blocks CO chemisorption at the axial  $\text{Cu}^{2+}$  position, as the  $2160\text{ cm}^{-1}$  shoulder in the gas phase is missing (spectra (1)-(3), Figure 5B), as is the  $\sim 2170\text{ cm}^{-1}$  feature in the chemisorbed phase (spectra (4)-(8)). As CO does not displace coordinated water, this is an indication the  $\text{Cu}^{2+}$  axial position binds water more strongly than CO.

Interestingly, residual water had little effect on CO chemisorption to the  $\text{Cu}^+$  site, as the  $\sim 2113\text{ cm}^{-1}$  feature remains in the chemisorbed phase (spectra (4) to (8), Figure 5B). The nature of the  $\text{Cu}^+$  defect site in Cu-BTC has been the subject of some debate, as discussed briefly above. Recent DFT calculations suggest the  $\text{Cu}^+$  feature is consistent with a missing ligand defect.<sup>22</sup> If this model is true, the retention of CO chemisorption to the  $\text{Cu}^+$  missing ligand defect would imply the missing ligand creates a hole that may accommodate CO, even as coordinated water is retained. As no change in porosity was detected in the  $\text{N}_2$  isotherms (Figure 3 and Figure S8), the number of these missing defects must be quite small.

**B(SA)** was then pretreated at a temperature (633 K for 15 minutes) close to the onset of thermal degradation ( $\sim 640\text{ K}$ , Figure S7) as an alternate (and more extreme) method to introduce defects. Examination of the full FTIR spectra (Figure S6B) demonstrates this high temperature pretreatment attacked the Cu-O bond without altering the ligand. Specifically, the Cu-O modes (at  $758\text{ cm}^{-1}$ ,<sup>26</sup> at  $1114\text{ cm}^{-1}$  and  $1706\text{ cm}^{-1}$ <sup>43</sup>) were decreased or eliminated; the C=O stretch of carboxylic acid ( $1215\text{ cm}^{-1}$ <sup>26,44</sup>) was partially regenerated; while the aromatic C=C (at  $1448\text{ cm}^{-1}$ ,  $1606\text{ cm}^{-1}$ ) and C-H features ( $3085\text{ cm}^{-1}$ <sup>45,46</sup>) were unperturbed. The degraded **B(SA)** showed no evidence of CO adsorption to the  $\text{Cu}^{2+}$  position, and virtually no CO

adsorption to the  $\text{Cu}^+$  position (Figure 5C). This demonstrates an intact Cu-O-C bond and/or an intact framework is necessary for CO chemisorption at the conditions of measurement. Although other Cu and Cu-O surfaces (e.g. the oxides and zeolites discussed in the introduction) may interact with CO, the retention of CO will be strongly dependent upon the adsorption conditions as well as gas accessibility to the surface sites.

### 3.2.3 CO perturbation by aged **B(RU)** Cu-BTC

**B(RU)** and **B(SA)** were synthesized on very different scales, yet no appreciable differences in any characterization results were noted between **B(RU)** and **B(SA)**. After storage for one year, **B(RU)**-1 had the following evidence for increased defects relative to the as-received **B(RU)**: (1) it had visibly changed color (See Figure S10), (2) it had a 10% reduction in surface area (Figure 3), and (3) a 5% increase in the fraction of  $\text{Cu}^+$  sites in XPS (Figure 4). Despite this, the  $\text{Cu}^{2+}/\text{Cu}^+$  FTIR peak ratio of **B(RU)**-1 was almost double that of **B(SA)** (blue spectra, Figure 5A and 5D, peak fitting in Figure S3, and parameters in Table S3, Supporting Information, which shows a  $\text{Cu}^{2+}/\text{Cu}^+$  peak ratio of 0.667 for **B(RU)**-1 and 0.375 for **B(SA)**). Thus, the FTIR spectra of chemisorbed CO did not follow the trends of the other characterization methods. The FTIR spectra of gas phase CO (red, Figure 5) show an apparent increase in the intensity of the  $2169\text{ cm}^{-1}$  peak in **B(SA)** relative to **B(RU)**-1. However, there was high variability in the intensity of this peak in subsequent measurements (see, e.g., “150 K\_CO”, in Figure 6 below), and thus, the intensity of the  $2169\text{ cm}^{-1}$  shoulder is a poor metric for defects.

To further explore the differences in FTIR of **B(SA)** versus **B(RU)-1**, the FTIR measurement was repeated with subsequent heating (in 0.34 bar Ar) to a number of discrete temperatures, for a combined temperature-desorption FTIR (TD-FTIR) measurement. For **B(SA)**, the CO chemisorbed to the  $\text{Cu}^{2+}$  site was retained up to  $\sim 200$  K (Figure 6), corresponding to an estimated activation energy of  $\sim 0.60$  eV (see Redhead Analysis, Table S2 Supporting Information). CO chemisorbed to the  $\text{Cu}^+$  site was retained up to  $\sim 400$  K (Figure 6), an activation energy of  $\sim 1.2$  eV (Supporting Information). Activation energies and binding energies are often assumed to be linearly related through the Brønsted-Evans-Polanyi rule,<sup>47,48</sup> and these trends are in qualitative agreement with the DFT binding energies calculated for adsorption of the first CO to  $\text{Cu}_2(\text{BTC})_4$  and  $\text{Cu}_2(\text{BTC})_3$ , i.e. 0.290 eV and 0.710 eV, respectively.<sup>22</sup> (The DFT calculated binding energies for the second CO adsorbed to  $\text{Cu}_2(\text{BTC})_4$  and  $\text{Cu}_2(\text{BTC})_3$  are 0.290 eV and 0.210 eV, respectively.) The shape of the CO vibrations remained symmetric for **B(SA)** as the temperature was increased. The only difference observed in the TD-FTIR of **B(RU)-1** was asymmetry in the CO spectra with heating. Without a more rigorous modeling study, we were unable to interpret these subtle differences in symmetry.

Overall, we were unable to use the CO FTIR technique to differentiate **B(RU)-1** from **B(SA)**, despite these two samples having notable differences in XPS,  $\text{N}_2$  BET surface area, and XRD. The CO FTIR measurement was able to detect defects introduced via residual “guest” species and those introduced via thermal degradation. We anticipate the XPS would be insensitive to these types of defects, although they would be apparent in  $\text{N}_2$  adsorption isotherms. Although prior DFT calculations suggest the intensity of the CO bound to the  $\text{Cu}^+$  defect site should have a five-fold

increased sensitivity relative to XPS,<sup>22</sup> our results suggest use of *in situ* FTIR is a less sensitive probe of defects relative to XPS and N<sub>2</sub> adsorption.

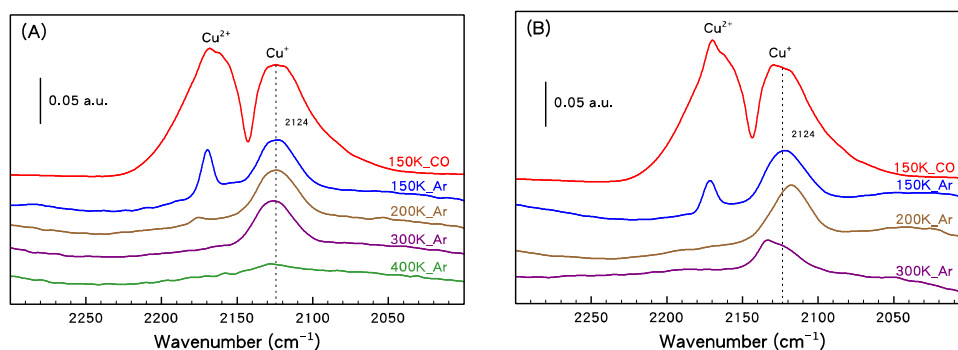


Figure 6. TPD-FTIR spectra of (A) **B**(SA) and (B) **B**(RU)-1 after a preliminary exposure in CO at 150 K (red; note that the intensity is normalized for clarity), followed by purging in Ar at 150K, then heating (in Ar) to 200 K (brown), 300 K (purple), and 400 K (green), as shown. The spectra shown represent data after no change was observed with time. The scale bar, a.u., denotes absorbance units.

### 3.3 In situ CO perturbation absent in the FTIR spectra of Cu-TDPAT

#### 3.3.1 Lack of CO perturbation by Cu-TDPAT

Somewhat surprisingly, measurement of the CO spectra in the presence of **T** led to no evidence for gas-phase CO perturbation or chemisorption after CO removal, despite the similar axial Cu<sup>2+</sup> adsorption site as **B** for CO chemisorption (Figure 7). Thus, there is no real evidence found in the *in situ* FTIR measurement for either physisorption or chemisorption of CO to **T**. The pores of **T**, as determined by the H-K method (Figure S8, Supporting Information), are 10-20 Å, large enough to easily

accommodate CO (with a kinetic diameter of  $3.76 \text{ \AA}^{49}$  and a Lennard-Jones diameter of  $3.763 \text{ \AA}^{50}$ ). We repeated the FTIR measurement at 100 K, yet did not observe residual CO chemisorption (Supporting Information, Table S1 and Figure S1), thus ruling out a lower CO binding energy in the **T** structure. We also varied the pretreatment conditions (from 373 to 573 K) to rule out the potential for residual water or thermal degradation to eliminate chemisorption to the axial  $\text{Cu}^{2+}$  position. We also attempted to introduce defects via grinding to magnify the CO adsorption signal (Supporting Information, Table S1). As no CO perturbation was found for any of the pretreatment conditions studied (see Supporting Information), the lack of CO chemisorption could not be attributed to residual water, thermal degradation, or insufficient defects.

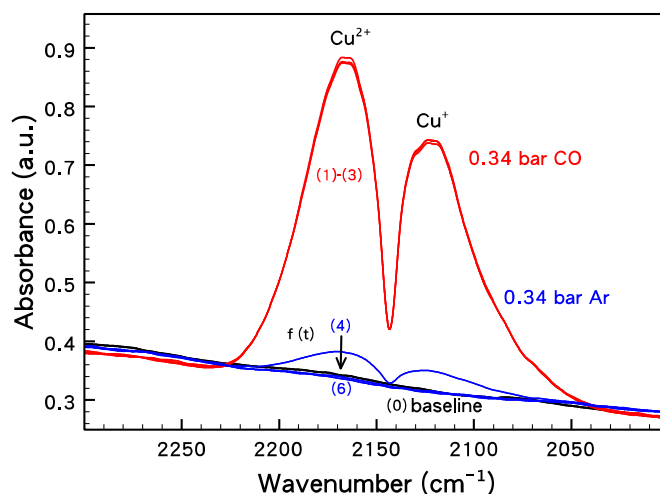


Figure 7. FTIR spectra of **T** at 150 K in excess CO exposure (1-3) and in Ar purging to remove gas phase CO for CO chemisorption (4-6). The number represents the sequence of each spectrum, where (0) was collected in Ar purging before the sample

was exposed to CO. No evidence for CO chemisorption was observed for any pretreatment temperature, adsorption temperature, or sample preparation method.

### 3.3.2 Ligand Induced Electron Density Effects

We compared the low wavenumber Cu-O stretch modes of **T** to **B** (Figure 8) to examine how the ligand may affect the electron density at the Cu<sup>2+</sup> axial adsorption site. Both the Cu-O stretch ( $\nu$ ) and bend ( $\delta$ ) modes of **B(SA)** are red-shifted by 10-15 cm<sup>-1</sup> relative to **T**, which corresponds to a decreased electron density of **T**. This has been demonstrated in studies that probe the nature of various coordinated organic molecules on the frequency of the Cu-O bond in mixed copper complexes.<sup>51</sup> As **T** has amino groups that are generally thought of as electron-donating, the decreased electron density of **T** (relative to **B(SA)**) appears to have more to do with the spatial density of the Cu paddlewheel than the nature of the organic functional groups of the ligand. The longer TDPAT ligand decreases the spatial density of the electron-rich Cu in **T**. An electron deficiency in **T** can also explain our observation for a high tendency for Cu reduction in Cu-TDPAT.<sup>38</sup> The effect of electron density is revisited below.

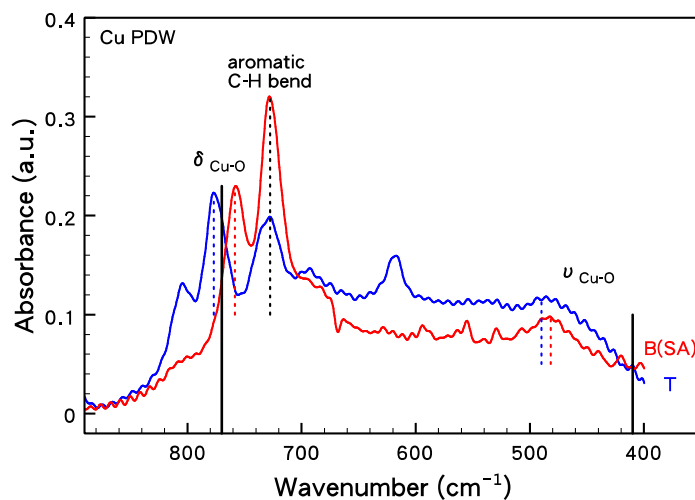


Figure 8. FTIR fingerprint region for Cu-TDPAT (**T**; blue) and Basolite (**B(SA)**; red) in Ar at 300K. Cu-O bond assignments are based on prior DFT calculations (black bars).<sup>38</sup> The C-H aromatic bend assignment is based on aromatic C-H bend at 750-800.<sup>45</sup> Notation is as follows:  $\delta$  = bend;  $\nu$  = stretch. A 10-15 wavenumber red shift is observed in the Cu-O bonds for **B(SA)** relative to **T**.

### 3.3.3 CO Adsorption and Desorption Isotherms

To better understand the lack of CO perturbation in the pores of **T**, we utilized gravimetric adsorption of CO at 77 K, followed by temperature-programmed-desorption (TPD) to 300 K. The CO adsorption isotherms of both **T** and **B(SA)** followed a general Langmuir shape, with a limiting surface coverage. When the CO adsorption is normalized per total pore volume (as measured by N<sub>2</sub> 77 K adsorption, Table 1), the density of chemisorbed CO retained in the pores of the two materials is similar at 0 bar (desorption) and 77 K (Figure 9, inset). Per unit Cu, **T** had higher CO adsorption than **B(SA)** at 77 K and all pressures studied (Figure 9).

Much of the CO accommodated within the pore of **T** is desorbed via pressure reduction at 77 K, suggesting the desorbed CO molecules are physisorbed. From Figure 9, 2.5 CO molecules (per Cu) are physisorbed to **T**, while 4.4 CO molecules (per Cu) are chemisorbed. In contrast, virtually all of the 3.4 CO molecules (per Cu) within the pores of **B(SA)** are retained upon pressure reduction at 77 K, and thus are attributed to chemisorption. Given the FTIR results above, it is notable that the amount of chemisorbed CO retained by **T** at 77 K is greater than that of **B(SA)**.

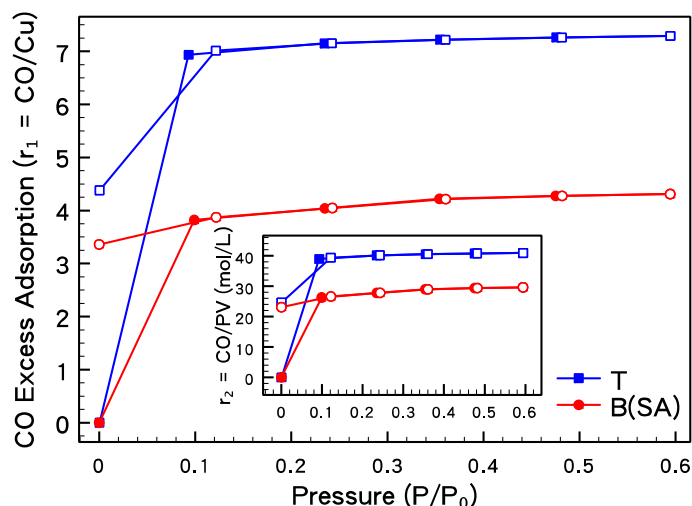


Figure 9. The CO 77 K adsorption-desorption (filled-empty symbol) isotherms of Cu-BTC (**B(SA)**; red) and Cu-TDPAT (**T**; blue) up to 0.34 bar ( $P/P_0 = 0.6$ , where  $P_0$  of CO = 0.58 bar at 77 K), which is the same total pressure as the FTIR experiments. Higher CO adsorption is observed in **T** than that in **B(SA)**.

### 3.3.4 Temperature-Programmed Desorption, 0 bar

This residual chemisorbed CO was desorbed by heating in vacuum to both estimate the amount of CO associated with the two structures at 150 K, and estimate the binding energy of the chemisorbed CO. Both **T** and **B(SA)** have similar bimodal TPD profiles (Figure 10). From 77 K to ~160 K the amount of chemisorbed CO is reduced to 1 in both **T** and **B(SA)**. The last CO (per Cu) is desorbed between 160 K and 210 K. The TD-FTIR (Figure 6) suggests this desorption can be attributed to  $\text{Cu}^{2+}$ , as CO bound to the  $\text{Cu}^+$  is retained up to 400 K. Thus, although amplified in FTIR, the  $\text{CO}-\text{Cu}^+$  is a very small fraction of the total CO adsorbed, and may be disregarded in subsequent discussion of the TPD.

Most notably, the TPD suggests both **T** and **B(SA)** will have (at least) one CO associated with the Cu axial position at vacuum and 160 K, a temperature exceeding that of the FTIR measurement. In fact, the TPD suggests more than one CO will bind to the Cu axial position at the conditions of the FTIR measurement, even in vacuum. Although prior studies do consider the possibility of multiple CO molecules per Cu site,<sup>28,35</sup> this has generally been considered at “high loading” (i.e.  $P \gg 0$ ) conditions only. These excess CO molecules are more readily desorbed than the final CO molecule that binds at the axial position.

Based on the corresponding CO:Cu ratio, the first TPD peak up to 160 K corresponds to “excess” CO molecules, i.e. those that exceed a 1:1 CO:Cu stoichiometric ratio. A Redhead analysis (See Equations S1-S5, Figure S5, and Table S2 Supporting Information) suggests the activation energy for desorption of these excess CO molecules is 0.4 eV. The second peak in the TPD profile corresponds to desorption of the final CO molecule that is more strongly bound to the  $\text{Cu}^{2+}$  axial position. A Redhead analysis shows this desorption temperature corresponds to an activation energy of 0.6 eV.

The similarity of the **T** and **B(SA)** TPD profiles suggest equivalent adsorption sites, indicating the chemisorbed CO is interacting with the Cu axial position rather than the ligand. In fact, when the TPD is normalized per pore volume, the TPD of the two materials is virtually indistinguishable (Figure 10, inset). This suggests the density of the residual CO in the two materials is similar, despite differences in pore structure. As the pore structures of **B(SA)** and **T** differ substantially (Figure 1), equal CO density implies either rearrangement of the CO molecules or flexibility of the structure under different gaseous environments.

Considering the final CO, **T** binds this more strongly than **B(SA)**, as the TPD profile is shifted to higher temperature (Figure 10). Estimated activation energies are 0.57 eV (for **B**) and 0.59 eV (for **T**; see Table S2 Supporting Information). This slight difference is likely attributed to differences noted in the electron density above. However, this minor difference is unlikely to explain the absence of CO perturbation in the FTIR spectra of **T**.

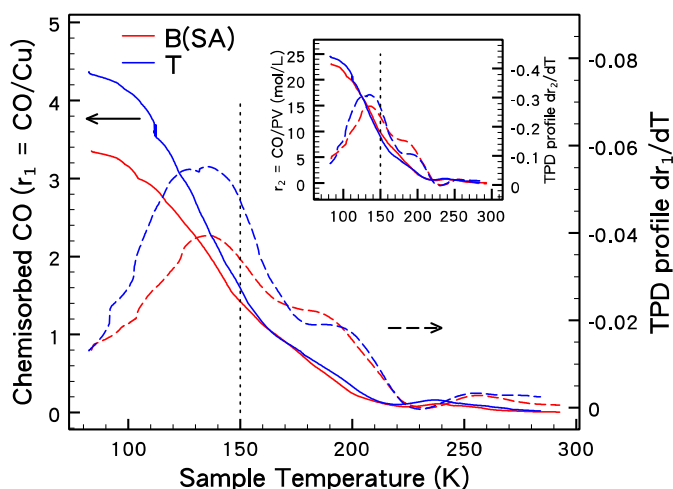


Figure 10. Temperature-programmed desorption (2 K/min) of CO after CO adsorption and desorption at 77 K for **B(SA)** (red) and **T** (blue), conducted in vacuum. Data in inset is reprocessed to pore volume ratio, based on the textural properties reported in Table 1.

### 3.3.5 Temperature-Programmed Desorption “Isobar” at 0.34 bar

The TPD experiment was repeated at 0.34 bar to better match the conditions of the FTIR measurement. This *isobar* desorption profile of **B(SA)** has an additional low temperature peak at ~100 K, but otherwise closely resembles the 0 bar TPD profile, albeit shifted to higher temperatures (Figure 11). At 0.34 bar, “excess” CO

(i.e. CO:Cu>1) is retained up to 230 K. The final CO is retained to almost 300 K. Once again, this is clear evidence that CO:Cu likely exceeds unity at the conditions of the FTIR measurement.

The **T** isobar differs markedly from that of **B(SA)**, as well as its own 0 bar TPD profile (Figure 11). Unlike **B(SA)**, no low-temperature peak is observed in the **T** isobar, despite more CO physisorption expected for **T** (Figure 9). The “excess” CO (i.e. CO:Cu>1) bound to **T** is desorbed by 230 K, but with no delineation in the binding energies. The broad and indistinct isobar profile of **T** suggests the CO molecules rearrange within the structure and are not associated with distinct binding sites. Above 230 K, removal of the final CO from **T** closely resembles **B**. Once again, this suggests the binding of the *final* CO molecule is fairly independent of the ligand or the pore structure.

Normalization of the isobar profiles by pore volume suggests the CO density retained in the pores differs at 0.34 bar up to ~180 K (Figure 11, inset). As this was not the case in the TPD, this suggests the presence of other gaseous molecules leads to a restructuring of the adsorbed layer or expansion of the substrate. Clearly, the CO adsorbed-phase density within the pores of **T** is affected by the gas over pressure. This is also consistent with the very broad pore-size distribution calculated from the N<sub>2</sub> isotherm (Supporting Information Figure S8): the N<sub>2</sub> molecules likely rearrange themselves leading to indistinct adsorption sites.

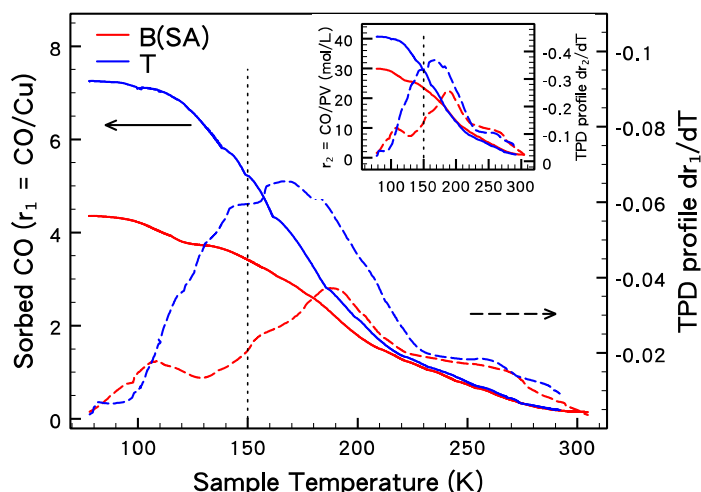


Figure 11. IGA-TPD profiles (isobar) of **B(SA)** (red) and **T** (blue) after CO adsorption isotherms at 77 K, 0.34 bar in molar ratio of CO/Cu and in CO to pore volume ratio (inset) with ramping rate 2 K/min. The solid curves indicate the profiles of molar ratio of CO to Cu, and the long dash lines show the derivatives individually. The short black dash line represents the working temperature 150 K in FTIR in Figure 5-6.

### 3.3.6 Discussion

In all cases, the amount of CO chemisorbed to the axial Cu position of **T** exceeds that of **B(SA)** up to temperatures well above 150 K, the temperature of the FTIR measurement. Thus, the lack of FTIR perturbation in **T** seen at 150 K certainly cannot be attributed to lack of CO adsorption.

The data above suggest the “excess” CO molecules are likely arranged differently in the two structures, yet retain at least partial association with the Cu axial position. An increased number of “excess” CO molecules in **T** likely corresponds to a larger CO-Cu distance to accommodate a greater number of CO molecules. Although

adsorption of “excess” CO will be driven by a thermodynamic incentive to decrease the free energy of the system, subsequent adsorbed CO molecules are expected to have a decreased binding energy, and may decrease the average binding energy *per CO molecule* for those adsorbed at low coverage. Accommodation of multiple CO may lead to a weakened CO-Cu interaction at high coverage, even as the overall energy is decreased. In other words, an increased number of CO molecules associated with the Cu adsorption site of **T** should decrease the electronic perturbation of any individual CO atom.

Alternatively, the absence of a CO perturbation for **T** may be due to the orientation of chemisorbed CO. The CO ligand is expected to bind to Cu either through a (i) CO-Cu sigma (terminal) bond (illustrated in Figure 12A), or through a (ii) CO-Cu  $\pi$ -backbonding arrangement (Figure 12B<sup>52</sup>). Both of these bonding arrangements will affect the C-O frequency, and lead to an IR-active dipole moment. Thus, either of these bonding arrangements can explain the CO spectra in the presence of **B**. In contrast, chemisorbed CO arranged in pairs that are bonded trans to one another about the Cu site will not be IR active due to a symmetric arrangement that lacks a dipole moment. One illustrative example (of perhaps many possible scenarios) is illustrated in Figure 12C. A symmetric bonding arrangement could explain the lack of CO perturbation observed in **T**. The retention of an even number of chemisorbed CO (i.e.  $\sim 4$ ) for **T** and an odd number of CO molecules for **B** ( $\sim 3$ ) at 77 K is consistent with this explanation. Another alternative is if surface selection rules led to IR inactivity, which would require CO to be oriented parallel to the incident beam.<sup>53,54</sup> For example, CO adsorbed parallel to a Pt electrode surface via a “bridging” configuration gives rise to FTIR-inactivity.<sup>55</sup> However, it seems highly

unlikely that all CO molecules in a porous, powdered, polycrystalline material would all have this orientation.

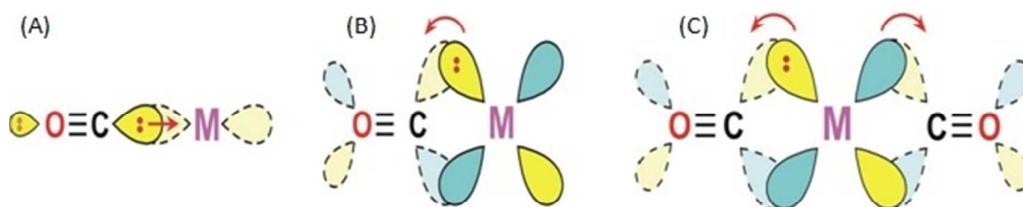


Figure 12: Possible bonding types for CO with Cu: (A) CO-M terminal sigma bond, and M to CO  $\pi$ -backbonding for (B) one and (C) two CO molecules. (A) and (B) would give rise to a dipole and thus be IR-active; the symmetric bonding arrangement in (C) would have no dipole and not be IR active. The specific structures are meant to be illustrative examples only.

Others have also suggested multiple CO molecules per Cu adsorption site on Cu-BTC,<sup>28,35</sup> although one group thought subsequent CO molecules were associated with unique adsorption sites on the ligand.<sup>29</sup> The similarity of TPD profiles for Cu-BTC with Cu-TDPAT suggest all CO are likely associated with the Cu axial position. The multiple COs are retained by the structure more strongly than that expected for physisorption to the ligand. Moreover, the TPD results demonstrate two distinct binding energies for the CO, associated with weakly bound “excess” CO molecules (CO:Cu>1) and a final CO (CO:Cu=1) that is bound more strongly. Notably, the adsorbed film is a dynamic function of temperature and pressure, even when chemisorbed.

#### 4. Summary and Conclusions

*In situ* FTIR of CO molecules adsorbed to Cu-BTC is an emerging technique to assess defects.<sup>21,22,28,35</sup> At low CO coverage, FTIR features at  $\sim 2120\text{ cm}^{-1}$  and  $2170\text{ cm}^{-1}$  are assigned to CO interacting with  $\text{Cu}^+$  and  $\text{Cu}^{2+}$  adsorption sites, respectively. Although DFT studies suggest this technique amplifies the  $\text{Cu}^+$  signal,<sup>22</sup> we found the technique to be relatively insensitive to  $\text{Cu}^+$  defects that were observed in XPS and evident via a reduced  $\text{N}_2$  adsorption, and more subtlety in PXRD.

The extension of the CO FTIR technique from Cu-BTC to Cu-TDPAT was not straightforward, despite similar Cu adsorption sites on the Cu paddlewheel. Although Cu-TDPAT adsorbed and retained more CO at all conditions studied, it had no perturbation in the *in situ* CO FTIR measurement. We attribute this to either a decrease in the relative binding energy per molecule and/or orientation of the CO molecules chemisorbed to the Cu axial position.

An *in situ* probe of gas-surface interactions in MOFs is not necessarily transferrable from one structure to another, even when the adsorption sites are similar. Thus, development of a site-specific, *in situ* probe of MOF defects will likely require development of a unique probe for each structure. The following factors must be taken into account: the potential for dynamic arrangement (and rearrangement) of the adsorbed layer as a function of temperature and gas-loading, the binding energy of the probe molecule as a function of loading, the temperature of the FTIR measurement, the electronic environment induced by the ligand, and the packing of the probe molecule next to the adsorption site. For CO adsorption to Cu-BTC and Cu-TPDAT, the latter had the greatest influence on the CO FTIR spectra.

## Acknowledgement

The initial spectroscopic measurements were supported by the U.S. Department of Energy, Energy Efficiency and Renewable Energy program, Award DE-FG36-08GO18139. Additional spectroscopic measurements, analysis, and adsorption studies were supported by the U.S. Department of Energy, Basic Energy Sciences Awards DE-FG02-09ER466556 and DE-SC0002157. The authors thank Jennifer Gray and Joshua Stapleton in Materials Characterization Lab at the Pennsylvania State University for the assistance in XPS and FTIR.

## Reference

- 1 M. Eddaoudi, J. Kim, N. Rosi, D. Vodak, J. Wachter, M. O'Keeffe, and O.M. Yaghi, *Science*, 2002, **295**, 469.
- 2 J. Moellmer, E.B. Celer, R. Luebke, A.J. Cairns, R. Staudt, M. Eddaoudi, and M. Thommes, *Micropor. Mesopor. Mat.*, 2010, **129**, 345.
- 3 X. Lin, N. Champness, and M. Schröder, Hydrogen, Methane and Carbon Dioxide Adsorption in Metal-Organic Framework Materials, 2010
- 4 H. Wu, Q. Gong, D.H. Olson, and J. Li, *Chem. Rev.*, 2012, **112**, 836.
- 5 P. Horcajada, C. Serre, M. Vallet-Regí, M. Sebban, F. Taulelle, and G. Férey, *Angew. Chem. Int. Ed.*, 2006, **45**, 5974.
- 6 M.P. Suh, Y.E. Cheon, and E.Y. Lee, *Coordin. Chem. Rev.*, 2008, **252**, 1007.
- 7 Z. Hu, B.J. Deibert, and J. Li, *Chem. Soc. Rev.*, 2014, **43**, 5815.
- 8 A. Corma, H. García, and F.X. Llabrés i Xamena, *Chem. Rev.*, 2010, **110**, 4606.
- 9 Y. Zhao, J. Zhang, J. Song, J. Li, J. Liu, T. Wu, P. Zhang, and B. Han, *Green Chem.*, 2011, **13**, 2078.
- 10 J.L.C. Rowsell and O.M. Yaghi, *Angew. Chem. Int. Ed.*, 2005, **44**, 4670.
- 11 H. Frost, T. Düren, and R.Q. Snurr, *J. Phys. Chem. B*, 2006, **110**, 9565.
- 12 D. Sun, S. Ma, Y. Ke, D.J. Collins, and H.C. Zhou, *J. Am. Chem. Soc.*, 2006, **128**, 3896.
- 13 Y.K. Hwang, D.Y. Hong, J.S. Chang, S.H. Jung, Y.K. Seo, J. Kim, A. Vimont, M. Daturi, C. Serre, and G. Férey, *Angew. Chem. Int. Ed.*, 2008, **47**, 4144.

- 14 W. Morris, R.E. Taylor, C. Dybowski, O.M. Yaghi, and M.A. Garcia-Garibay, *J. Mol. Struct.*, 2011, **1004**, 94.
- 15 W.X. Cao, Y.W. Li, L.M. Wang, and S.J. Liao, *J. Phys. Chem. C*, 2011, **115**, 13829.
- 16 K.L. Mulfort and J.T. Hupp, *Inorg. Chem.*, 2008, **47**, 7936.
- 17 H. Wu, Y.S. Chua, V. Krungleviciute, M. Tyagi, P. Chen, T. Yildirim, and W. Zhou, *J. Am. Chem. Soc.*, 2013, **135**, 10525.
- 18 G. Barin, V. Krungleviciute, O. Gutov, J.T. Hupp, T. Yildirim, and O.K. Farha, *Inorg. Chem.*, 2014, **53**, 6914.
- 19 Z. Wang, H. Sezen, J. Liu, C. Yang, S.E. Roggenbuck, K. Peikert, M. Fröba, A. Mavrantoukakis, B. Supronowicz, and T. Heine, *Micropor. Mesopor. Mat.*, 2015, **207**, 53.
- 20 Y. Mao, L. Shi, H. Huang, Q. Yu, Z. Ye, and X. Peng, *Cryst. Eng. Comm.*, 2013, **15**, 265.
- 21 O. Shekhah, J. Liu, R.A. Fischer, and C.h. Wöll, *Chem. Soc. Rev.*, 2011, **40**, 1081.
- 22 P. St Petkov, G.N. Vayssilov, J. Liu, O. Shekhah, Y. Wang, C. Wöll, and T. Heine, *Chem. Phys. Chem.*, 2012, **13**, 2025.
- 23 D. Saha and S. Deng, *Int. J. Hydrogen Energ.*, 2009, **34**, 2670.
- 24 O. Kozachuk, I. Luz, F.X. Llabrés i Xamena, H. Noei, M. Kauer, H.B. Albada, E.D. Bloch, B. Marler, Y. Wang, M. Muhler, and R.A. Fischer, *Angew. Chem. Int. Ed.*, 2014, **53**, 7058.

- 25 J. Hafizovic, M. Bjørgen, U. Olsbye, P.D. Dietzel, S. Bordiga, C. Prestipino, C. Lamberti, and K.P. Lillerud, *J. Am. Chem. Soc.*, 2007, **129**, 3612.
- 26 C.Y. Wang, J.L. Gray, Q. Gong, Y. Zhao, J.o.h.n. Li, E. Klontzas, G. Psofogiannakis, F. Froudakis, and A.D. Lueking, *J. Phys. Chem. C*, 2014, **118**, 26750.
- 27 C.S. Tsao, M.S. Yu, C.Y. Wang, P.Y. Liao, H.L. Chen, U.S. Jeng, Y.R. Tzeng, T.Y. Chung, and H.C. Wu, *J. Am. Chem. Soc.*, 2009, **131**, 1404.
- 28 L. Alaerts, E. Séguin, H. Poelman, F. Thibault-Starzyk, P.A. Jacobs, and D.E. De Vos, *Chemistry*, 2006, **12**, 7353.
- 29 N. Drenchev, E. Ivanova, M. Mihaylov, and K. Hadjiivanov, *Phys. Chem. Chem. Phys.*, 2010, **12**, 6423.
- 30 J. Szanyi, M. Daturi, G. Clet, D.R. Baer, and C.H. Peden, *Phys. Chem. Chem. Phys.*, 2012, **14**, 4383.
- 31 S.S.-Y. Chui, S.M.-F. Lo, J.P. Charmant, A.G. Orpen, and I.D. Williams, *Science*, 1999, **283**, 1148.
- 32 A. Vishnyakov, P.I. Ravikovitch, A.V. Neimark, M. Bülow, and Q.M. Wang, *Nano Lett.*, 2003, **3**, 713.
- 33 M.B. Seasholtz, L.E. Pence, and O.A. Moe, *J. Chem. Educ.*, 1988, **65**, 820.
- 34 K.I. Hadjiivanov, M.M. Kantcheva, and D.G. Klissurski, *J. Chem. Soc., Faraday Trans.*, 1996, **92**, 4595.
- 35 S. Bordiga, L. Regli, F. Bonino, E. Groppo, C. Lamberti, B. Xiao, P.S. Wheatley, R.E. Morris, and A. Zecchina, *Phys. Chem. Chem. Phys.*, 2007, **9**, 2676.

- 36 B. Li, Z. Zhang, Y. Li, K. Yao, Y. Zhu, Z. Deng, F. Yang, X. Zhou, G. Li, H. Wu, N. Nijem, Y.J. Chabal, Z. Lai, Y. Han, Z. Shi, S. Feng, and J. Li, *Angew. Chem. Int. Ed.*, 2012, **51**, 1412.
- 37 M. Schlesinger, S. Schulze, M. Hietschold, and M. Mehring, *Micropor. Mesopor. Mat.*, 2010, **132**, 121.
- 38 C.Y. Wang, Q. Gong, Y. Zhao, J. Li, and A.D. Lueking, *J. Catal.*, 2014, **318**, 128.
- 39 S. Brunauer, P.H. Emmett, and E. Teller, *J. Am. Chem. Soc.*, 1938, **60**, 309.
- 40 F. Rouquerol, J. Rouquerol, and K.S.W. Sing, Adsorption by powders & porous solids: principles, methodology and applications, 1999
- 41 J.F. Moulder and J. Chastain, Handbook of X-Ray Photoelectron Spectroscopy: A Reference Book of Standard Spectra for Identification and Interpretation of XPS Data, 1992
- 42 Z.Q. Li, L.G. Qiu, T. Xu, Y. Wu, W. Wang, Z.Y. Wu, and X. Jiang, *Mater. Lett.*, 2009, **63**, 78.
- 43 N.A.A. Sani, W.J. Lau, and A.F. Ismail, *RSC Advances*, 2015, **5**, 13000.
- 44 X.M. Liu, S. Rather, Q. Li, A.D. Lueking, Y. Zhao, and J. Li, *J. Phys. Chem. C*, 2012, **116**, 3477.
- 45 *Infrared spectroscopy correlation table*
- 46 G. Mahalakshmi and V. Balachandran, *Spectrochim Acta A*, 2014, **124**, 535.
- 47 J.N. Bronsted *Chem. Rev.*, 1928, **5**, 231.
- 48 M.G. Evans and M. Polanyi, *T Faraday Soc.*, 1938, **34**, 11.

49 R.W. Triebe and F.H. Tezel, *Gas Sep. Purif.*, 1995, **9**, 223.

50 R.S. Berry, S.A. Rice, and J. Ross, *Physical Chemistry*, 2000

51 L. Gasque, G. Medina, L. Ruiz-Ramírez, and R. Moreno-Esparza, *Inorg. Chim. Acta*, 1999, **288**, 106.

52 *Organometallic Chemistry*

53 R.G. Greenler *J Chem. Phys.*, 1966, **44**, 310.

54 Y.J. Chabal *Surf. Sci. Rep.*, 1988, **8**, 211.

55 Y. Ikezawa, H. Saito, H. Fujisawa, S. Tsuji, and G. Toda, *J. Electroanal. Chem.*, 1988, **240**, 281.